Journal of Catalysis **200,** 288–297 (2001)
doi:10.1006/jcat.2001.3184, available online at http://www.idealibrary.com on IDEAL®

Role of HY Zeolite Mesopores in Hydrocracking of Heavy Oils

Koichi Sato,*[,1] Yoichi Nishimura,* Kosaku Honna,† Nobuyuki Matsubayashi,* and Hiromichi Shimada*

*National Institute of Materials and Chemical Research, 1-1 Higashi, Tsukuba, Ibaraki 305-8565, Japan; and †Tsukuba Branch, Advanced Catalysts Research Laboratory, Petroleum Energy Center, 1-1 Higashi, Tsukuba, Ibaraki 305-8565, Japan

Received October 2, 2000; revised December 22, 2000; accepted January 3, 2001; published online May 15, 2001

Two kinds of NiMo/HY catalysts, with and without mesopores, were prepared starting from two NaY zeolites with different Si/Al ratios. Both catalysts possessed similar properties arising from micropores because the catalysts had similar zeolitic framework structures. For both catalysts, most of the NiMo sulfides were dispersed inside the micropores. The remaining NiMo sulfides, being relatively large particles (3–10 nm), were located on the mesopore surface for the NiMo/HY with mesopores, whereas for the NiMo/HY without mesopores, they were located on the external surface of zeolite particles. The catalytic activities were evaluated by the hydrocracking of tetralin and atmospheric residue. Both catalysts showed similar catalytic performance in the hydrocracking of tetralin, which diffused into the micropores. In the hydrocracking of atmospheric residue, however, NiMo/HY with mesopores was superior to that without mesopores. These results revealed the important role of mesopores as active catalytic sites in the hydrocracking of heavy oils.

Key Words: **Y-type zeolite; NiMo/HY; external surface; mesopore; hydrocracking; tetralin; heavy oil.**

1. INTRODUCTION

Hydrocracking is one of the most promising processes for producing valuable petroleum products from heavy oils. In hydrocracking, Y-type zeolite-based catalysts have many advantages over amorphous SiO_2–Al_2O_3 catalysts, namely, high activity, low coke formation, high resistance against nitrogen compounds, and high regenerability (1). An intrinsic problem of Y-type zeolite catalysts, however, is the inability of large molecules to diffuse into the 0.74-nm-diameter micropores. Therefore, active catalytic sites are limited to the external surface.

External surfaces of Y-type zeolites are classified into two categories: the external surface of zeolite particles, and the mesopore surface that is formed during ion exchange and dealumination procedures (2). Past studies on the external surfaces of Y-type zeolites predominantly dealt with the external surface of zeolite particles, for example, by comparing the catalytic activities of zeolites with different particle sizes using model compounds (3), vacuum gas oil (4), and heavy gas oil (5). Those reports did not discuss in detail the active catalytic sites on the mesopore surface. However, the external surface areas of zeolite particles with an average diameters of $\sim$1 μm are quite small, and thus the majority of the catalytic sites for large molecules are located on the mesopore surfaces. The role of mesopores in the reactions of large molecules has been empirically recognized in the catalytic cracking or hydrocracking processes (6). Nevertheless, there have been very few studies on the mesopores of Y-type zeolites, probably due to the complexity of the catalytic properties of Y-type zeolites with great mesoporosity.

The final goal of our research group is to develop Y-type zeolite catalysts with proper mesoporosity that are favorable for the hydrocracking of heavy oils. For this purpose, the catalytic properties and activities of the mesopores of Y-type zeolites must be clarified. In a previous study, we prepared two kinds of HY zeolites, with and without mesopores, starting from two kinds of NaY zeolites, and then evaluated their cracking activity using two model compounds of different molecular size (7). The results clearly indicated that the mesopores of Y-type zeolites played an important role in the cracking of large molecules that cannot diffuse into the micropores.

In our current study, we prepared two kinds of NiMo-supported zeolite catalysts using the above-mentioned HY zeolites, with and without mesopores, starting from two kinds of NaY zeolites. We then evaluated the catalytic activities of the two NiMo catalysts in the hydrocracking of heavy oil and tetralin. The results revealed the important role of mesopores in the hydrocracking of heavy oils over zeolite-supported NiMo sulfide catalysts. In addition, problems of zeolite-supported NiMo sulfide catalysts in the hydrocracking of heavy oils are discussed on the basis of the results of detailed characterization of the catalysts.

[1] To whom correspondence should be addressed. Fax: +81-298-61-4534. E-mail: ksato@nimc.go.jp.

0021-9517/01 $35.00

2. EXPERIMENTAL

2.1. Preparation of Catalysts

Two kinds of NaY zeolites were used as starting materials: NaY(TO) with a framework Si/Al ratio of 2.8 supplied from Tosoh Corp. and NaY(CE) with a framework Si/Al ratio of 4.1 prepared in our laboratory by hydrothermal synthesis using 15-crown-5 as a template (8). The HY zeolites were obtained by ion exchange cycles using an aqueous solution of ammonium sulfate (3 mol/l) at 368 K for 1 h, followed by drying at 393 K for 12 h and calcining in dry air at 873 K for 3 h. This ion exchange cycle was repeated 3 or 4 times so that the final Na concentration was less than 0.6 wt%. The total amount of ammonium sulfate in the ion exchange solution was 1.7 equiv for the first cycle and 3.0 equiv for subsequent cycles. Further details of the zeolite synthesis were described previously (7).

NiMo/HY catalysts ($NiO = 1.7$ wt%, $MoO_3 = 6.7$ wt%) were prepared by the following impregnation method using aqueous solutions of ammonium heptamolybdate ($(NH_4)_6Mo_7O_{24}$:AHM) and nickel nitrate ($Ni(NO_3)_2$). After the Mo impregnated zeolites were dried at room temperature, Ni impregnation was done, followed by drying at 393 K for 12 h and calcination at 823 K for 3 h. All the drying and calcination procedures were done under ambient atmospheric conditions. Prior to the characterization and reaction tests, each NiMo/HY catalyst was sulfided with a flow of 5% H_2S/H_2 gas under atmospheric pressure for 2 h at 673 K.

Molybdenum dithiocarbamate ($[(C_8H_{17})_2NC])_2S_6Mo_2O_2$:MoDTC), an oil-soluble organic metal complex, was chosen as a reference catalyst, because MoDTC had no cracking function but exhibited high performance in the hydroprocessing of heavy oils.

2.2. Characterization of Catalysts

The porosity of each sample was determined by measuring the N_2 isotherm at 77 K with a Micromeritics ASAP 2010. The total surface area was calculated by using the BET method. The external surface area and micropore volume were calculated by using the *t*-plot method. Note that this calculated external surface area contains both the mesopore surface area and the external surface area of the zeolite particles. The micropore surface area was obtained by subtracting the calculated external surface area from the calculated total surface area. The pore size distribution profile was calculated by using the BJH method with the N_2 desorption isotherm (9). The mesopore volume was obtained by integrating the differential pore volume in Fig. 2 for the pores with the diameter ranging from 2 nm to 50 nm.

The relative crystallinity and unit cell parameter of zeolite were calculated from the X-ray diffraction (XRD) patterns that were recorded with a MAC Science MXP-18 diffractometer and Cu$K\alpha$ radiation (0.1542 nm). The relative crystallinity was estimated by comparing the intensities of the six peaks respectively assigned to (331), (511), (440), (533), (642), and (555) reflections. The unit cell parameters were calculated from the (533) and (642) reflection peak positions that were determined using the (101) reflection peak of TiO_2 (anatase) as an internal standard.

The framework Si/Al ratio was obtained from the above unit cell parameters by using Breck's equation when the Si/Al ratio was smaller than 3 (10) and by using Engelhardt's relation when it was larger than 3 (11). The bulk Si/Al ratio was determined by inductively coupled plasma emission spectroscopy. The Na content was measured by atomic absorption analysis.

The acid properties were measured with an FT-IR instrument (Japan Spectroscopic Co., Ltd. FT/IR-5MP) using pyridine as a probe molecule. The measurement procedures were as follows. The sample (about 12.5 mg) was weighed and pressed into a self-supporting 10-mm-diameter wafer. After evacuation of the cell in a transmission IR cell at 673 K for 2 h, 400 Pa of pyridine was introduced into the cell at 423 K for 5 min. The physisorbed pyridine was removed by evacuation at the same temperature for 30 min. The IR spectrum was recorded at a resolution of 4 cm^{-1}. The amounts of Brønsted and Lewis acid sites were determined by the absorbance at 1543 and 1453 cm^{-1}, respectively.

The dispersion of NiMo sulfide on HY zeolite was estimated by the chemisorption of NO using a pulse-type reactor with a thermal conductivity detector (TCD). After the catalyst was sulfided under the above-described conditions (flow of 5% H_2S/H_2 gas under atmospheric pressure for 2 h at 673 K), the physisorbed H_2S was removed by flowing He at 673 K for 0.5 h. Pulses of 10.2 wt% NO gas with a volume of 2.0 cm^3 (9.1×10^{-6} mol) were introduced at 303 K to the catalyst at 2-min intervals until the catalyst surface was saturated with NO. The dispersion was calculated by dividing the number of moles of adsorbed NO by that of Mo.

The local structure around the Mo atoms was determined from extended X-ray absorption fine structure (EXAFS). The Mo K-edge EXAFS was measured at the BL-10B of the Photon Factory at the High Energy Accelerator Research Organization (Tsukuba, Japan). The catalyst was pressed into a self-supporting wafer, which was sulfided in a glass cell with Kapton windows under the above-described conditions (flow of 5% H_2S/H_2 gas under atmospheric pressure for 2 h at 673 K). After purging of the cell by N_2, the measurement was done at room temperature in the transmission mode without exposing the sample to air. The radial distribution function around Mo was obtained by Fourier transformation of the $k/f(k)$-weighted EXAFS. The detailed procedure for this transformation was described elsewhere (12).

The morphology of NiMo sulfide was observed by transmission electron microscopy (TEM). The samples were

TABLE 1

Properties of AR

Density (288 K, g/cm^3)	0.983
Sulfur content (wt%)	4.22
Nitrogen content (wt%)	0.27
Nickel content (ppm)	29
Vanadium content (ppm)	92
Asphaltene (wt%)	7.70

prepared by embedding the catalyst powders in epoxy resin at 338 K, followed by slicing using an ultramicrotome. The thickness of each sample was about 100 nm.

The chemical state and composition at the external surface of particle of the catalyst were measured by X-ray photoelectron spectroscopy (XPS) using a PHI-5500 spectrometer with monochromated Al$K\alpha$ radiation (1486.3 eV). The chemical composition was calculated using the peak areas and the atomic sensitivity factor given by the manufacturer (13).

2.3. Hydrocracking Reactions

Hydrocracking of tetralin as a model compound was done using a batch-type reactor whose inner volume was 50 cm^3. An autoclave with an electric furnace was waved with a rocking system during the reaction. The experimental conditions were as follows: 5 ml of tetralin, 0.3 g of catalyst, initial hydrogen pressure of 5.9 MPa (cold charge), reaction temperature of 623 K, and reaction time of 5 min to 60 min. The liquid products were analyzed using gas chromatography (GC) with an FID detector (Hewlett-Packard 6890)with a methylsilicon capillary column (Hewlett-Packard Ultra #1, 0.20 mm $\times$ 25 m). The gas products were analyzed with TCD-GC (Hewlett-Packard 6890).

For the hydrocracking of heavy oil, Arabian-heavy atmospheric residue (AR) was chosen as a feedstock. The properties of AR are listed in Table 1. A batch-type reactor whose inner volume was 140 ml was used for the reaction. The experimental conditions were as follows: 10 g of feedstock, 1 g of catalyst, initial hydrogen pressure of 9.8 MPa (cold charge), reaction temperature of 683 K, and reaction time of 3 h and 6 h. The liquid products were analyzed by high-temperature simulated distillation chromatography (AC Analytical Controls SIMDIS HT-750). The gas products were analyzed by the above-described TCD-GC. The amount of asphaltene was determined by measuring the *n*-heptane-insoluble materials. The sulfur and nitrogen contents were measured using a sulfur and nitrogen analyzer (APS Technology, Inc. APS35).

3. RESULTS AND DISCUSSION

3.1. Characterization of HY Zeolites

Table 2 summarizes the characterization results for the NaY and HY zeolites. The Na content in NaY(TO) was reduced to less than 0.3 wt% by three cycles of ion exchange. The unit cell parameter simultaneously decreased from 2.463 nm of NaY-type to 2.452 nm of HY-type due to dealumination from the zeolitic framework. The estimated change in the framework Si/Al ratio was from 2.8 of NaY-type to 5.0 of HY-type. In contrast, 0.56 wt% of Na remained in HY(CE) after four cycles of ion exchange of NaY(CE), despite the lower Na content in the starting material. During the ion exchange procedure, the Si/Al ratio of the framework changed from 4.1 to 5.3. These results indicate that in NaY(TO), the Na ions were relatively easily exchanged, together with dealumination from the framework, whereas in NaY(CE), the Na ion exchange and dealumination did not easily occur. As a result, the difference in the framework Si/Al ratios between HY(TO) and HY(CE) was relatively small compared to that between NaY(TO) and NaY(CE).

For both HY zeolites, the bulk Si/Al ratios were much lower than those of the framework. In addition, the relative crystallinities of the HY zeolites were about 80% of their corresponding NaY zeolites. These results indicate that the extracted Al species from the framework during ion exchange remained in the HY zeolite particles.

The surface area and pore volume of the micropores of NaY(TO) were similar to those of NaY(CE), because both zeolites had the same framework structure. For both

TABLE 2

Characterization of Zeolites

Zeolite	Na content (wt%)	Unit cell parameter (nm)	Si/Al molar ratio		Relative crystallinity (%)[a]	Surface area (m^2/g)		Pore volume (cm^3/g)		Acidity	
			Framework	Bulk		Micropore	External	Micropore	Mesopore	Brønsted	Lewis
NaY(TO)	7.09	2.463	2.8	2.9	100	707	46	0.33	0.068		
HY(TO)	0.27	2.452	5.0	3.2	80	644	122	0.30	0.114	0.76	0.77
NaY(CE)	6.14	2.457	4.1	3.6	124(100)	716	38	0.33	0.015		
HY(CE)	0.56	2.450	5.3	3.7	101(81)	628	57	0.29	0.026	0.77	0.57

[a] NaY(TO) was selected as a standard. The value in parentheses indicates the relative crystallinity referred to NaY(CE).

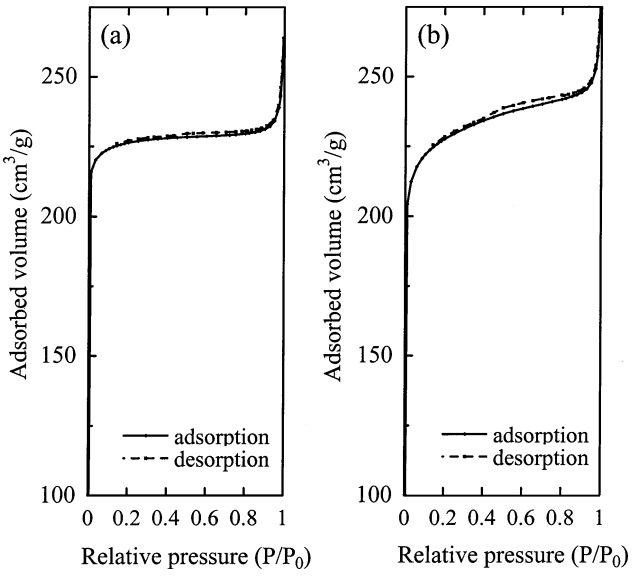

FIG. 1. N_2 isotherm. (a) NaY(TO), (b) HY(TO).

zeolites, the ion exchange reduced these values by about 10%, which was about half of the decreases in the crystallinity. Table 2 indicates evident changes in the external surface area and mesopore volume during the ion exchange cycles. The changes were particularly significant for NaY(TO). As a result of these ion exchange cycles, the mesopore volume of HY(TO) was about 4 times larger than that of HY(CE). Figure 1 compares the isotherms of NaY(TO) and HY(TO). The increase in the adsorbed volume with the relative pressure between 0.05 and 0.9 and the large hysteresis observed for HY(TO) corresponds to the larger mesopore volume of HY(TO).

Figure 2 shows the changes in the pore size distribution profiles of the zeolites. NaY(TO) had a small mesopore volume with mesopore diameters ranging from 2 nm to 50 nm whereas NaY(CE) had no mesoporosity. The ion exchange increased the mesopore volume of both zeolites.

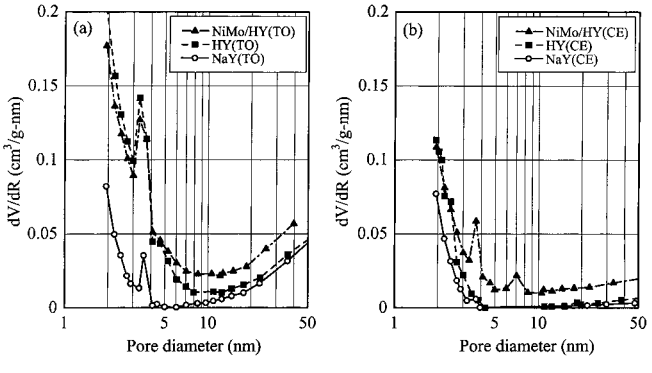

FIG. 2. Pore size distribution calculated by using the BJH method with the N_2 desorption isotherm. (a) Y(TO), (b) Y(CE).

The increase in the mesopore volume of Y(CE), however, was smaller than that of Y(TO). In fact, Fig. 2 shows that the change in the mesopore volume of Y(CE) with ion exchange was negligibly small, as compared with that of Y(TO). By SEM observation (7), the morphology of the particles for either zeolite remained relatively unchanged during the ion exchange cycle. These observations suggest that the increase in the external surface area of HY(TO) was due to the formation of mesopores inside the zeolite particles.

The acid properties of HY zeolites are listed in Table 2. The Brønsted acidity of HY(TO) was similar to that of HY(CE). This similarity is due to the similar framework structure and similar Si/Al ratios for HY(TO) and HY(CE), because Brønsted acid sites originate from the Al atoms in zeolite framework structures. Extraframework Al_2O_3 species, which are produced by extraction of aluminum oxide from the zeolite framework, are known to function as Lewis acid sites (14). The higher Lewis acidity of HY(TO) is likely due to the larger amount of extraframework Al_2O_3 in HY(TO).

In summary, two kinds of HY zeolites had similar properties arising from the zeolite framework structure. Compared with HY(CE), HY(TO) possessed significantly larger mesopore volume and extraframework Al_2O_3. The SEM photographs showed that the extraframework Al_2O_3 was not located as bulk on the external surfaces of the particles. However, possible locations of extraframework Al_2O_3, such as inside micropores or inside mesopores, need further study.

3.2. Characterization of NiMo/HY Catalysts

3.2.1. Framework structure. The physical and chemical properties of NiMo/HY catalysts are listed in Table 3. The unit cell parameters of the two NiMo/HY catalysts did not differ significantly from those of HY zeolites given in Table 2; the unit cell parameter of HY(TO) decreased from 2.452 to 2.449 nm, and that of HY(CE) from 2.450 to 2.449 nm. These changes were much smaller than those observed from NaY type to HY type. This indicates that the framework Si/Al ratios of the zeolites did not change during the NiMo loading. The loading of NiMo sulfide, however, resulted in a decrease in relative crystallinity of both zeolites. The crystallinities of NiMo/HY(TO) and NiMo/HY(CE) were 70% and 77%, respectively, of that before loading (Table 3).

This decrease in crystallinity was partly due to the X-ray absorption by Ni and Mo. Leglise *et al.* (15) calculated (by using XRD) the effect of Mo on the estimated crystallinity. On the basis of their calculations, the intrinsic crystallinity (C_i) of zeolite with 6.7 wt% of Mo was obtained by multiplying the experimentally obtained crystallinity (C_e) by a factor of 0.83. To confirm their calculations, we measured the crystallinity of physical mixtures of zeolite with 6.7 wt%

TABLE 3

Characterization of NiMo/HY Catalysts

Catalyst	Unit cell parameter (nm)	Framework Si/Al molar ratio	Relative crystallinity (%)[a]	Surface area (m^2/g)		Pore volume (cm^3/g)		Metal dispersion NO/Mo (mol/mol)
				Micropore	External	Micropore	Mesopore	
NiMo/HY(TO)	2.449	5.6	53 (70)	467	112	0.20	0.125	0.15
NiMo/HY(CE)	2.449	5.6	77 (77)	497	63	0.21	0.054	0.18

[a] NaY(TO) was selected as a standard. The value in parentheses indicates the relative crystallinity referred to each HY type.

of MoO_3 and MoS_2. The resulting C_i/C_e ratio was 0.83 for MoO_3 and 0.84 for MoS_2, consistent with the calculation by Leglise *et al.* These results indicate that in our experiments the intrinsic crystallinity of HY zeolites decreased by about 10–15% due to NiMo loading.

For both catalysts, the loading of NiMo sulfide decreased the surface area and pore volume arising from micropores by about 30%. The external surface area and mesopore volume of HY(TO) were not significantly changed by NiMo loading, whereas the mesopore volume of HY(CE) increased from 0.026 to 0.054 cm^3/g by NiMo loading. The pore size distribution profiles (Fig. 2) show that the mesopore distribution of NiMo/HY(TO) was similar to that of HY(TO), whereas the mesopore volume of Y(CE) with diameters ranging from 2–50 nm increased after NiMo loading. However, the mesopore volume of NiMo/HY(CE) was still about half that of NiMo/HY(TO).

These results indicate that NiMo loading resulted in the destruction of zeolite framework and in the formation of mesopores, particularly in HY(CE), although dealumination from the framework was not significant. Cid *et al.* (16–18) reported that the interaction between AHM (used in the impregnation of zeolites) and zeolite likely destroyed the zeolite structure during the calcination procedures. The possible destruction of the framework during the presulfidation cannot be excluded as suggested by Welters *et al.* (19).

3.2.2. Dispersion and location of NiMo sulfide. The Mo3*d* XPS spectra of two NiMo/HY catalysts are shown in Fig. 3. The peaks at 229.3 eV and 232.3 eV with spin orbital coupling ($Mo3d_{5/2}$ and $Mo3d_{3/2}$) were assigned to Mo^{4+} of MoS_2. The curve-fitting results of the spectra indicate almost no contribution from Mo^{6+}. Other parameters obtained form XPS spectra are summarized in Table 4. The S*2p* binding energies of 162.2–162.4 eV indicate that all the sulfur species in the catalysts were present as metal sulfides. The peak $Ni2p_{3/2}$ at 853.6 eV was assigned to nickel sulfide, possibly Ni_3S_2 or NiS. For both catalysts, the S/Mo ratio of about 2 shows that the Mo species at the external surface of zeolite particles was MoS_2. The Mo/(Si + Al) ratio of NiMo/HY(CE) was 3 times higher than that of NiMo/HY(TO). This indicates that Mo sulfides were more concentrated at the external surface of zeolite particles in NiMo/HY(CE) than in NiMo/HY(TO). For NiMo/HY(TO) the Mo/(Si + Al) ratio observed by XPS was smaller than the calculated ratio of the bulk, whereas for NiMo/HY(CE) that ratio observed by XPS was slightly higher than the calculated ratio of the bulk. Both NiMo/HY catalysts showed similar Ni/(Si + Al) ratios, which were almost equal to that of the bulk (0.017). Considering the experimental error, the distribution of Ni from the surface to the bulk can be assumed to be almost even for both catalysts.

Fourier transforms of Mo K-edge EXAFS spectra of the two NiMo catalysts are shown in Fig. 4. Both spectra showed two intense peaks, respectively corresponding to Mo–S ($r = 0.24$ nm) and Mo–Mo ($r = 0.32$ nm) scattering, but showed no peak assignable to Mo–O scattering. The average coordination number of Mo–Mo was estimated using the following relation (20, 21),

$$N(Mo) = BIr^2,$$

where I is the peak intensity of Mo–Mo scattering, r is the distance between the Mo atoms, and B is the proportionality

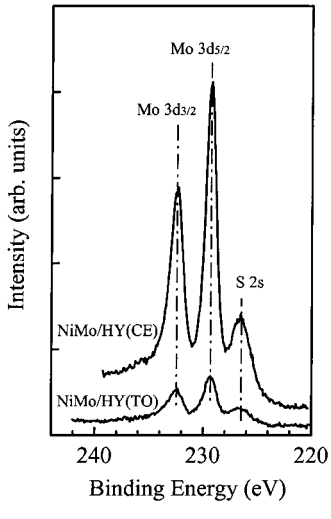

FIG. 3. Mo3*d* XPS spectra of NiMo/HY catalysts.

TABLE 4

XPS Measurements of NiMo/HY Catalysts

Catalyst	Peak energy (eV)			Molar ratio[a]			
	Mo3*d*	Ni2*p*	S2*p*	S/Mo	Mo/(Si + Al)	Ni/(Si + Al)	Ni/(Mo + Ni)
NiMo/HY(TO)	229.3	853.6	162.4	1.6	0.017 (0.035)	0.014 (0.017)	0.45
NiMo/HY(CE)	229.3	853.8	162.2	1.9	0.045 (0.034)	0.017 (0.017)	0.27

[a] The numbers in parentheses show the ratio in the bulk.

constant for Mo–Mo scattering obtained from MoS_2 crystals that have six Mo atoms around another Mo atom. Note that this relation assumes that the thermal and static disorders are constant. For both NiMo/HY catalysts, the calculated N(Mo) was 2.6. Using the relationship between the N(Mo) and crystallite size of MoS_2 (22) that included the effect of distortion and disorder of crystals (22, 23), we estimated that the average MoS_2 particle size was approximately 2 nm.

Table 3 shows the dispersion of NiMo sulfide analyzed by using NO chemisorption. The dispersion on HY(TO) was 0.15, whereas that on HY(CE) was 0.18. These values are larger than those reported previously on Mo/NaY with similar metal content (24, 25).

The characterization results of EXAFS and NO chemisorption give "average information" about NiMo sulfide in the catalysts. In contrast, TEM images give local but clear information about the morphology of MoS_2 particles as shown in Fig. 5. For both catalysts, the TEM images show that MoS_2 particles aggregated with stacked layers. The number of layers was about 5 to 10, which is greater than those reported for Al_2O_3-supported catalysts in many previous studies (26–30). The length of the particle layers was from 3 nm to 10 nm, which is also larger than those reported for Al_2O_3-supported catalysts in many previous reports (26–30). These observations in Fig. 5 are not consistent with the EXAFS and NO chemisorption results.

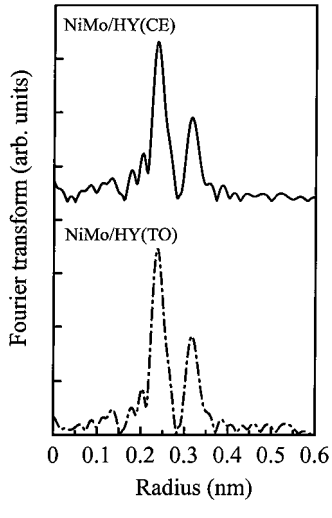

FIG. 4. Fourier transforms of the Mo K-edge EXAFS spectra for NiMo/HY catalysts.

Both catalysts presumably contained two kinds of MoS_2 particles: small clusters located inside the zeolite framework, and large particles located on the external surface. The small clusters were located in the micropores, either sodalite cage or supercage (31), and could not be observed by TEM. When catalysts were prepared starting from $Mo(CO)_6$ that can penetrate into micropore (24, 32), almost all of the MoS_2 clusters were located in the micropores. In the catalysts that we prepared from AHM, the $Mo_7O_{24}^{6-}$ anion that is formed in the first step of impregnation cannot penetrate the micropores. Due to calcinations above 623 K, however, Mo species migrate into the micropores (16, 18, 19, 33, 34). This migration results in the majority of MoS_2 clusters being located inside the micropores, as evidenced by relatively large NO chemisorption values (Table 3) and small average particle size estimated from EXAFS.

As discussed above, no significant differences between NiMo/HY(CE) and NiMo/HY(TO) were observed in the dispersion of MoS_2 clusters inside the micropores. The difference in the surface Mo/(Si + Al) ratios determined by XPS was caused by different locations of the *large* MoS_2 particles. The major part of the *large* MoS_2 particles observed in the TEM photographs (Fig. 5) are presumably located on the external surface of zeolite particles. In the case of NiMo/HY(TO), however, some of those particles with relatively small sizes are located inside the mesopores. It should be noted that the different locations of Mo sulfide particles between the two catalysts do not affect the average dispersion estimated by NO chemisorption and EXAFS, because the main contribution to the average dispersion is that of the MoS_2 clusters inside the micropores. The more significant aggregation of MoS_2 on zeolite than that on Al_2O_3 support (30) might be related to the weak interaction between Mo species and zeolite when the Si/Al ratio is high.

In contrast to the Mo/(Si + Al) ratio, both catalysts show similar Ni/(Si + Al) ratios in the XPS analysis. Due to the smaller size of Ni cations formed during the impregnation, the distribution of Ni in the zeolite particles was even,

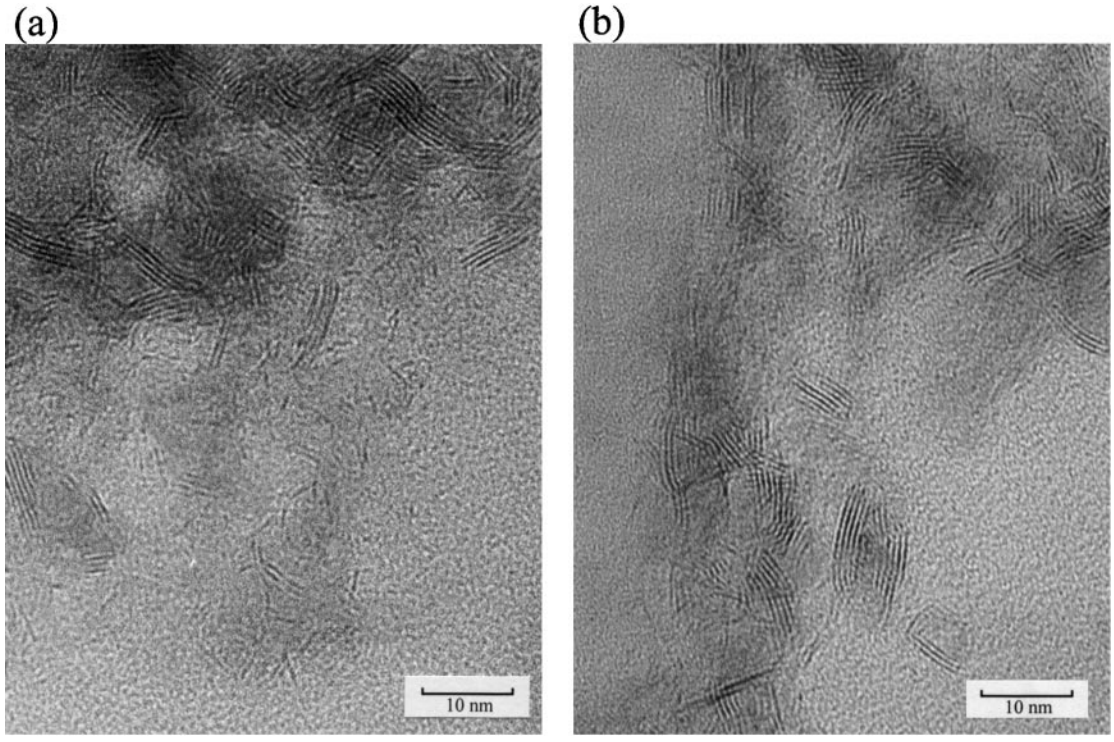

FIG. 5. TEM photographs of NiMo/HY catalysts. (a) NiMo/HY(TO), (b) NiMo/HY(CE).

irrespective of the presence or absence of mesopores. Inside micropores, it is very likely that MoS_2 clusters form cata lytically active "Ni–Mo–S" structure (35) as indicated by Leglise *et al*. For the large MoS_2 particles, however, the Ni/(Mo + Ni) ratios measured by XPS were different in the two zeolites. Further study is needed to clarify if these large MoS_2 particles form the Ni–Mo–S structure.

As discussed in Section 3.2.1, NiMo loading caused destruction of the zeolite framework. However, the difference in mesoporosity between two HY zeolites was preserved after the loading of NiMo sulfide, because the destruction was not significant. For both catalysts, most of the NiMo sulfides were small clusters located in the micropores, and the remainder were relatively large-size particles located on the external surface of the zeolite particles for NiMo/HY(CE) or on the mesopore surface for NiMo/HY(TO).

3.3. Hydrocracking of Tetralin

Table 5 shows the reaction rate and product distribution in the hydrocracking of tetralin. According to our previous study (36), the products were classified into the following groups: gas, monocyclic compounds, dicyclic compounds, and heavy compounds. Dicyclic compounds were further classified into decalin, decalin isomers, indan, methylindan, and naphthalene. The majority of the heavy compounds were partially hydrogenated tricyclic compounds and phenylbutyltetralin.

TABLE 5

Reaction Rate and Product Distribution of Tetralin Hydrocracking

			Reaction for 1 h						
			Product distribution (%)						
					Dicyclic				
Catalyst	Rate per total surface area (mol m^{-2} min^{-1})	Tetralin conversion (%)	Gas	Monocyclic	Decalin	Decalin isomers	Indan, methylindan	Naphthalene	Heavy
NiMo/HY(TO)	1.74×10^{-6}	49.4	2.3	26.2	3.5	8.8	7.1	2.5	49.6
NiMo/HY(CE)	1.63×10^{-6}	44.9	2.2	25.1	3.8	7.9	7.1	3.6	50.3

The reaction rate per unit surface area for NiMo/HY(TO) was about 7% higher than that for NiMo/HY(CE). As we previously reported (36), the effect of pore diffusional limitation is not significant under the reaction conditions that we studied here, according to the calculation using the Thiele modulus. Thus, tetralin molecules can diffuse into the micropores of Y-type zeolite. The similar catalytic activities for both NiMo/HY catalysts are presumably due to their similar catalytic properties arising from the micropore structures, namely, the framework Si/Al ratio, Brønsted acidity, and metal dispersion on the micropores. The slightly higher activity of NiMo/HY(TO) to the larger mesoporosity might enhance the diffusion of tetralin into the Y-type micropores. However, the similar product distributions over the NiMo/HY catalysts suggest that the effect of mesopores was small, if any.

Table 5 shows that both NiMo/HY catalysts yielded about 50% of heavy compounds. These heavy compounds were produced by aromatic electrophilic substitution reactions when dissociative hydrogen was not sufficiently supplied from NiMo sulfide to the acid sites (36). Although an HY zeolite-based catalyst showed better performance than other zeolites in the hydrocracking of tetralin (37), the high yields of heavy compounds in our study indicate an imbalance between the acidity of zeolitic framework and the hydrogen supply ability of NiMo sulfide. FT-IR measurements (Table 2) showed that both HY zeolites had relatively high Brønsted acidity. The catalysts that we studied here showed relatively high dispersion of NiMo sulfide (Table 3), but still could not supply sufficient hydrogen to compensate for the high densities of the acid sites. The similar yields of heavy compounds over the two NiMo/HY catalysts suggest that the mesoporosity did not play an important role in the suppression of these coke precursors.

3.4. *Hydrocracking of AR*

Table 6 shows the product distribution in the hydrocracking of AR with and without catalysts. The reaction without catalyst increased the asphaltene content and yielded a small amount of gaseous products. The addition of MoDTC significantly depressed the formation of asphaltene and slightly decreased the gas production, compared with the reaction without catalyst. In addition, MoDTC showed high HDS and HDN activities (Table 6). Figure 6a shows the distillation profiles of the feedstocks and the liquid products without a catalyst and with MoDTC. When no catalyst was used, thermal cracking shifted the distillation profile lower. When MoDTC was added, the shift in the profile was similar to that without a catalyst. As shown in Fig. 7,

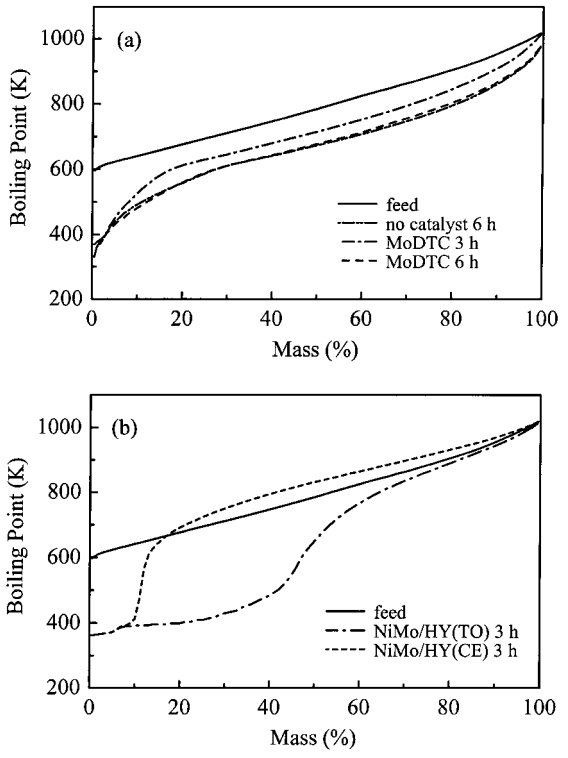

FIG. 6. Distillation curve of the products from the hydrocracking of AR. (a) Reactions without catalyst and over MoDTC, (b) reactions over NiMo/HY(TO) and NiMo/HY(CE).

TABLE 6

Hydrocracking of AR

	Reaction time (h)	Product distribution (wt%)			HDS activity (%)	HDN activity (%)
		Gas	Liquid	Asphaltene		
Feed	—	0	92.3	7.7	—	—
No catalyst (thermal cracking)	6	3.5	87.4	9.1	1.3	4.6
MoDTC	3	2.1	97.2	0.67	58.6	35.6
MoDTC	6	2.5	96.6	0.95	77.0	52.3
NiMo/HY(TO)	3	16.2	74.9	6.4	52.0	26.8
NiMo/HY(CE)	3	19.6	72.3	7.3	33.3	12.7

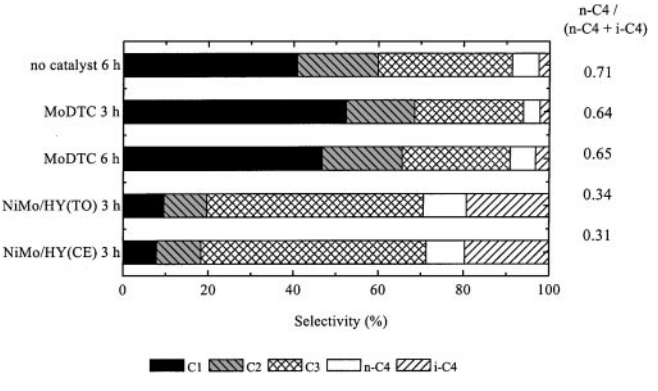

FIG. 7. Distribution of the gaseous products from the hydrocracking of AR.

the distribution of gas products over MoDTC was the same as that without a catalyst. Therefore, these results indicate that MoDTC functioned mainly as a hydrogenation and hydrotreating catalyst that slightly depresses the cracking reactions, which are due to the supply of hydrogen.

The product distributions over the zeolite-based catalysts were quite different from those over MoDTC (Table 6); both zeolite-based catalysts produced larger amounts of gaseous products and asphaltene yields than did catalysts with MoDTC. In addition, compared with thermal reaction or MoDTC (Fig. 7), the zeolite-based catalysts had low selectivity to methane and high selectivity to iso-C_4 relative to normal-C_4. This distribution was characteristic of catalytic hydrocracking on acid sites via carbenium cation (38). Note that NiMo/HY(CE) produced slightly more gas products and higher asphaltene yields than did NiMo/HY(TO) (Table 6).

In contrast to the similar gas product distributions for NiMo/HY(TO) and NiMo/HY(CE), comparison of the two distillation profiles indicates that NiMo/HY(TO) was superior to NiMo/HY(CE) in hydrocracking performance, particularly in the yields of the fraction under 700 K (Fig. 6b). The entire profile for NiMo/HY(TO) shifted downward, whereas for NiMo/HY(CE), the profile shifted upward above 600 K. These results indicate that unfavorable hydrocracking reactions that led to gas production occurred in a similar manner over both zeolite-based catalysts, whereas favorable hydrocracking that produced light and middle distillates was catalyzed only over NiMo/HY(TO). Table 6 also shows that higher HDS and HDN activities were obtained over NiMo/HY(TO) than over NiMo/HY(CE), although those activities were lower than those over MoDTC.

The above reaction results indicate that the function of the mesopores of NiMo/HY(TO) was to hydrocrack large molecules and to remove heteroatoms. In contrast, the function of the micropores was gas production, and thus both zeolite-based catalysts produced similar yields and product distributions of gaseous materials. When small molecules were produced by thermal cracking or catalytic cracking over the external surface, these molecules entered the micropores and were further hydrocracked to gaseous molecules.

As indicated by XPS (3.2.2), NiMo sulfides were dispersed on the mesopore surface of NiMo/HY(TO), which served two functions, namely, hydrogenation and hydrocracking of large molecules. In NiMo/HY(CE), however, the active sites for large molecules were limited to the external surface of zeolite particles, resulting in the observed differences in the catalytic performance in distillation profiles, HDS and HDN. Our previous model reaction results involving large-size molecules suggested that the cracking rate per area over the mesopore surface was faster than that over the external surface of zeolite particles (7). This faster rate might be due to the effect of mesopore as a "specific field;" namely, porous structures are more effective for catalysis than are flat surfaces. As discussed in Section 3.1., HY(TO) contained a larger amount of extraframework Al_2O_3 and thus possessed large Lewis acidity. In addition, the Ni/(Mo + Ni) ratios of NiMo sulfide particles between NiMo/HY(TO) and NiMo/HY(CE) were different. These different characters between two zeolites might have affected their catalytic performances. However, these differences were presumably relatively insignificant, because both catalysts exhibited similar performances in the hydrocracking of tetralin. Therefore, we conclude that the differences in the distillation profiles of the products over the two catalysts are, for the most part, attributed to the different mesopore structures.

The advantages of NiMo/HY(TO) over NiMo/HY(CE) in the reaction of AR are as follows: (i) zeolitic mesopores provide favorable active catalytic sites for large molecules, and (ii) well-dispersed NiMo sulfides on the mesopore surface supply dissociative hydrogen species that enhance not only hydrocracking but also heteroatom removal from large molecules.

The NO adsorption results suggest that the dispersion of NiMo sulfides in the catalysts that we studied was relatively high. However, the hydrocracking of AR over the NiMo sulfide catalysts resulted in high yields of asphaltene (Table 6). Furthermore, the hydrocracking of tetralin over the NiMo sulfide catalysts also resulted in high yields of heavy compounds (Table 5). The production of these unsuitable products was likely due to the imbalance between cracking and hydrogenation activities of the catalysts, in other words, insufficient interaction between cations produced on the acid sites and dissociatively adsorbed hydrogen produced on NiMo sulfide. The solid acid density of the HY (Al/Si $\sim$ 0.2) that we studied might have been too high for hydrocracking AR. As evidenced by the TEM photograph (Fig. 5), some Mo sulfide aggregated and formed particles as large as 10 nm. This means that the dispersion of NiMo sulfide can be improved.

In the hydrocracking of AR, although the functionality of NiMo/HY(TO) catalyst was significantly superior to that of NiMo/HY(CE), it was not sufficient for hydrocracking the fraction over 850 K. The mesopores of NiMo/HY(TO) were presumably not large enough to accommodate the heaviest fractions. To improve the catalytic performance of HY-based hydrocracking catalysts, more precise control of mesopore structures is required in addition to the control of acid density and the improvement of the dispersion of NiMo sulfide.

4. CONCLUSION

In this study, we prepared and characterized two kinds of NiMo/HY catalysts with and without mesopores starting

from two NaY zeolites with different Si/Al ratios. Both zeolites were found to possess similar properties arising from micropore structure, namely, micropore surface area, micropore volume, framework Si/Al ratio, and Brønsted acidity, whereas the two catalysts were found to have different mesopore structures. For both catalysts, the majority of NiMo sulfides were dispersed in the micropores of zeolites. In the NiMo/HY(TO) with mesopores, NiMo sulfides were also located inside the mesopores, whereas in the NiMo/HY(CE), NiMo sulfides were deposited on the external surface of zeolite particles.

In the hydrocracking of tetralin, no significant difference was observed in the catalytic activities of the two NiMo/HY catalysts. These similar activities were due to the similar catalytic properties arising from micropores, because tetralin molecules could diffuse into the micropores. In the hydrocracking of AR, compared to NiMo/HY(CE) without mesopores, NiMo/HY(TO) with mesopores showed superior performance in middle or light oil yields and heteroatom removal. In gas production, however, both catalysts showed similar results. These results on the hydrocracking of heavy oils indicate that the mesopore surface of NiMo/HY(TO) played an important role in hydrocracking heavy fractions, whereas the micropores played a major role in the gas production.

As evidenced by the large yield of heavy compounds in the hydrocracking of tetralin, the hydrogen supply from NiMo sulfides to acid sites was not sufficiently fast to stabilize the intermediate cations. Further interaction between hydrogenation active sites and acid sites is needed to reduce unfavorable retrogressive reactions during the hydrocracking of heavy oils. Furthermore, minimization of acidity in the micropore surface is essential to suppress the gas production.

ACKNOWLEDGMENTS

This work has been financially supported by Petroleum Energy Center with the subsidy of the Ministry of International Trade and Industry.

REFERENCES

1. Maxwell, I. E., *Catal. Today* **1**, 385 (1987).
2. Scherzer, J., *ACS Symp. Ser.* **248**, 157 (1984).
3. Auguar, E. F. S., Valle, M. L. M., Silva, M. P., and Silva, D. F., *Zeolites* **15**, 620 (1995).
4. Camblor, M. A., Corma, A., Martinnez, A., Mocholi, F. A., and Pariente, J. P., *Appl. Catal.* **55**, 65 (1989).
5. Rajagopalan, K., Peters, A. W., and Edwards, G. C., *Appl. Catal.* **23**, 69 (1986).
6. Shimada, H., Yoshitomi, S., Sato, T., Matsubayashi, N., Imamura, M., Yoshimura, Y., and Nishijima, A., *Stud. Surf. Sci. Catal.* **106**, 115 (1997).
7. Sato, K., Nishimura, Y., and Shimada, H.,*Catal. Lett.* **60**, 83 (1999).
8. Delprato, F., Delmotte, L., Guth, J. L., and Huve, L., *Zeolites* **10**, 546 (1990).
9. Barrett, E. P., Joyner, L. S., and Halenda, P. P., *J. Am. Chem. Soc.* **73**, 373 (1951).
10. Breck, D. W., "Zeolites Molecular Sieves," p. 94 Wiley, New York, 1974.
11. Fichtner-Schmittler, H., Lohse, U., Engelhardt, G., and Patzeloua, V., *Cryst. Res. Technol.* **19**, K1 (1984).
12. Matsubayashi, N., Shimada, H., Imamura, M., Yoshimura, Y., Nishijima, A., Calais, C., and Geantet, C., *J. Synchrotron Rad.* **6**, 428 (1999).
13. Wagner, C. D., Riggs, W. M., Davis, L. E., Moulder, J. F., and Muilenberg, G. E., "Handbook of X-Ray Photoelectron Spectroscopy." Perkin-Elmer, Eden Prairie, MN, 1979.
14. Loeffler, E., Lohse, U., Peuker, Ch., Oehlmann, G., Kustov, L. M., Zholobenko, V. L., and Kazansky, V. B., *Zeolites* **12**, 175 (1992).
15. Leglise, J., Manoli, J. M., Potvin, C., Djega-Mariadassou, G., and Cornet, D., *J. Catal.* **152**, 275 (1995).
16. Cid, R., Llambias, F. J. G., Fierro, J. L. G., Agudo, A. L., and Villasenor, J., *J. Catal.* **89**, 478 (1984).
17. Agudo, A. L., Cid, R., Orellana, F., and Fierro, J. L. G., *Polyhedron* **5**, 187 (1986).
18. Fierro, J. L. G., Conesa, J. C., and Agudo, A. L., *J. Catal.* **108**, 334 (1987).
19. Welters, W. J. J., Vorbeck, G., Zandbergan, H. W., Ven, L. J. M., Oers, E. M., Haan, J. W., Beer, V. H. J., and Santen, R. A., *J. Catal.* **161**, 819 (1996).
20. Stern, E. A., Sayers, D. E., and Lytle, F. W., *Phys. Rev. B* **11**, 1009 (1975).
21. Shimada, H., Matsubayashi, N., Sato, T., Yoshimura, Y., Imamura, M., Kameoka, T., and Nishijima, A., *Catal. Lett.* **20**, 81 (1993).
22. Shido, T., and Prins, R., *J. Phys. Chem. B* **102**, 8426 (1998).
23. Calais, C., Matsubayashi, N., Geantet, C., Yoshimura, Y., Shimada, H., Nishijima, A., Lacroix, M., and Breysse, M., *J. Catal.* **174**, 130 (1998).
24. Okamoto, Y., Maezawa, A., Kane, H., and Imanaka, T., *J. Mol. Catal.* **52**, 337 (1989).
25. Laniecki, M., and Zmierczak, W., *Zeolites* **11**, 18 (1991).
26. Delnmay, F., *Appl. Catal.* **16**, 135 (1985).
27. Ramirez, J., Fuentes, S., Diaz, G., Vrinat, M., Breysse, M., and Lacroix, M., *Appl. Catal.* **52**, 211 (1989).
28. Pratt, K. C., Sanders, J. V., and Christov, V., *J. Catal.* **124**, 416 (1990).
29. Eijsbouts, S., Heineman, J. J. L., and Elzerman, H. J. W., *Appl. Catal. A: General* **105**, 53 (1993).
30. Payen, E., Hubaut, R., Kasztelan, S., Poulet, O., and Grimbrot, J., *J. Catal.* **147**, 123 (1994).
31. Li, D., Nishijima, A., and Morris, D. E., *J. Catal.* **182**, 339 (1999).
32. Okamoto, Y., Katsuyama, H., Yoshida, K., Nakai, K., Matsuo, M., Sakamoto, Y., Yu J., and Terasaki, O., *J. Chem. Soc., Faraday Trans.* **92**, 4647 (1996).
33. Welters, W. J. J., Waerden, O. H., Zandbergan, H. W., Beer, V. H. J., and Santen, R. A., *Ind. Eng. Chem. Res.* **34**, 1156 (1995).
34. Thoret, J., Marchal, C., Doremieux-Morin, C., Man, P. P., Gruia, M., and Fraissard, J., *Zeolites* **13**, 269 (1993).
35. Leglise, J., Janin, A., Lavalley, C., and Cornet, D., *J. Catal.* **114**, 388 (1988).
36. Sato, K., Iwata, Y., Miki, Y., and Shimada, H., *J. Catal.* **186**, 45 (1999).
37. Sato, K., Iwata, Y., Yoneda, T., Nishijima, A., Miki, Y., and Shimada, H., *Catal. Today* **45**, 367 (1998).
38. Plank, C. J., Sibbett, J., and Smith, R. B., *Ind. Eng. Chem.* **49**, 742 (1957).